Journal of Pharmaceutical Analysis 13 (2023) 24–38

Contents lists available at ScienceDirect

Journal of Pharmaceutical Analysis

journal homepage: www.elsevier.com/locate/jpa

Original article

Epigenetic drug library screening reveals targeting DOT1L abrogates NAD^+ synthesis by reprogramming H3K79 methylation in uveal melanoma

Xiang Gu [1], Yu Hua [1], Jie Yu [1], Ludi Yang [1], Shengfang Ge, Renbing Jia, Peiwei Chai***, Ai Zhuang**, Xianqun Fan*

Department of Ophthalmology, Shanghai Key Laboratory of Orbital Diseases and Ocular Oncology, Shanghai Ninth People's Hospital, Shanghai Jiao Tong University School of Medicine, Shanghai, 200011, China

ARTICLE INFO

Article history:
Received 15 July 2022
Received in revised form
16 November 2022
Accepted 22 November 2022
Available online 28 November 2022

Keywords:
Histone methylation
Metabolic reprogramming
Uveal melanoma
Transcriptional addiction

ABSTRACT

Uveal melanoma (UM) is the most frequent and life-threatening ocular malignancy in adults. Aberrant histone methylation contributes to the abnormal transcriptome during oncogenesis. However, a comprehensive understanding of histone methylation patterns and their therapeutic potential in UM remains enigmatic. Herein, using a systematic epi-drug screening and a high-throughput transcriptome profiling of histone methylation modifiers, we observed that disruptor of telomeric silencing-1-like (DOT1L), a methyltransferase of histone H3 lysine 79 (H3K79), was activated in UM, especially in the high-risk group. Concordantly, a systematic epi-drug library screening revealed that DOT1L inhibitors exhibited salient tumor-selective inhibitory effects on UM cells, both in vitro and in vivo. Combining Cleavage Under Targets and Tagmentation (CUT&Tag), RNA sequencing (RNA-seq), and bioinformatics analysis, we identified that DOT1L facilitated H3K79 methylation of nicotinate phosphoribosyltransferase (NAPRT) and epigenetically activated its expression. Importantly, NAPRT served as an oncogenic accelerator by enhancing nicotinamide adenine dinucleotide (NAD^+) synthesis. Therapeutically, DOT1L inhibition epigenetically silenced NAPRT expression through the diminishment of dimethylation of H3K79 (H3K79me2) in the *NAPRT* promoter, thereby inhibiting the malignant behaviors of UM. Conclusively, our findings delineated an integrated picture of the histone methylation landscape in UM and unveiled a novel DOT1L/NAPRT oncogenic mechanism that bridges transcriptional addiction and metabolic reprogramming.

1. Introduction

Transcriptional addiction is a hallmark of oncogenesis, and epigenetic alterations result in pronounced global remodeling of the transcriptional landscape [1]. Histone methylation, an essential modification that coordinates the maintenance of epigenetic homeostasis, regulates spatial organizations of chromosomes during transcription [2]. Aberrant histone methylation patterns conferring transcriptional remodeling underlie tumorigenesis and tumor evolution [3]. For example, the fusion of histone 3 lysine 36 (H3K36) methyltransferase nuclear receptor-binding SET domain protein 1 to nucleoporin-98 in acute myeloid leukemia results in enhanced trimethylated H3K36 at the homeobox A cluster (HOXA) gene locus, stimulating HOXA transcription and promoting oncogenesis [4]. Moreover, histone demethylase lysine-specific demethylase 1 (LSD1) co-localizes with the androgen receptor (AR) and motivates AR-dependent transcription by demethylation of histone H3 lysine 9 (H3K9) to relieve repressive histone marks in prostate cancer. An LSD1 inhibitor blocks demethylation of H3K9, abolishes androgen-induced transcriptional activation, and suppresses tumor growth [5]. Therefore, pharmacological targeting of histone methylation regulators is a potential therapeutic strategy in cancer and warrants further investigation.

Uveal melanoma (UM), the most frequent and aggressive ocular malignancy in adults, presents with high rates of metastasis and mortality [6]. The prognosis of metastatic UM is poor with a median progression-free survival time of 3.3 months [7]. UM was identified by gene expression profiling into two molecular subtypes: one

Peer review under responsibility of Xi'an Jiaotong University.
* Corresponding author.
** Corresponding author.
*** Corresponding author.
E-mail addresses: chaipeiwei123@sjtu.edu.cn (P. Chai), aizh9h@163.com (A. Zhuang), fanxq@sjtu.edu.cn (X. Fan).
[1] These authors contributed equally to this work.

https://doi.org/10.1016/j.jpha.2022.11.008

related to monosomy 3 with poor prognosis and high risk of metastases, while the other related to disomy 3 (D3) with better prognosis and low risk of metastases [8]. Strikingly, chemotherapy and immunotherapy are less effective in UM treatment, which is in contrast to the favorable responses in cutaneous melanoma [9]. Hence, employing novel molecular bases of UM progression and developing intervention strategies are critical priorities. Although the histone H3 lysine 27 methyltransferase enhancer of zeste 2 polycomb repressive complex 2 subunit (EZH2) has been reported to facilitate the development of UM [10,11], whether EZH2 is a druggable target for UM is still controversial. LaFave et al. [12] suggested that loss of BRCA1-associated protein 1 (BAP1) function results in EZH2-dependent transformation in cancers with BAP1 deficiency. In contrast, Schoumacher et al. [13] proposed that the expression of EZH2 does not differ significantly between samples with wild-type and mutated BAP1 and that UM cells are impervious to EZH2 inhibition irrespective of their BAP1 status. Currently, the pattern of histone methylation during UM progression remains to be fully illuminated.

In this study, we systematically analyzed the pattern of histone methylation in UM and tested the inhibitory efficacy of histone methylation inhibitors in UM. As a result, we identified that histone 3 lysine 79 (H3K79) methyltransferase disruptor of telomeric silencing-1-like (DOT1L) was tumor-specifically upregulated, conferring vulnerability towards DOT1L inhibitors. Targeted correction of aberrant DOT1L expression and H3K79 methylation exhibited therapeutic efficacy by attenuating nicotinate phosphoribosyltransferase (NAPRT) transcription and nicotinamide adenine dinucleotide (NAD^+) synthesis. Our findings provide insights into a novel mechanism of DOT1L-guided transcriptional dysregulation in tumorigenesis and offer a promising therapeutic intervention in UM.

2. Material and methods

2.1. Clinical samples

In all, six human UM tissues, three human nevus tissues, and four human uvea tissues were obtained from Department of Ophthalmology, Shanghai Ninth People's Hospital, Shanghai Jiao Tong University School of Medicine (Shanghai, China).

2.2. Cell lines

The cell lines 92-1 and MUM2B were from human UM supplied by Professor John F. Marshall (Centre for Tumor Biology, Queen Mary University of London, London, UK). The cell lines MEL285, MEL290, OMM1, and OMM2.3 were provided by Professor Martine J. Jager (Department of Ophthalmology, Leiden University Medical Center, Leiden, the Netherlands). The cell line HEK293T was obtained from the American Type Culture Collection (Manassas, VA, USA). The cell line PIG1 from human normal melanocyte was obtained from Department of Ophthalmology, Peking University Third Hospital (Beijing, China). Short tandem repeat profiling was used to authenticate all cell lines. MUM2B and HEK293T cells were cultured in DMEM (Gibco, Waltham, MA, USA). PIG1, 92-1, MEL285, MEL290, OMM1, and OMM2.3 cells were cultured in Gibco RPMI 1640. All cells were cultured in media with streptomycin (100 mg/mL), penicillin (100 U/mL), and 10% fetal bovine serum (Gibco) with 5% CO_2 at 37 °C.

2.3. Histone methylation inhibitor screening

The histone methylation inhibitors used for screening were purchased from Selleck (Shanghai, China). OMM2.3, 92-1, and PIG1 cells were screened in parallel with inhibitors at a concentration of 10 μM in 96-well plates (Corning, Glendale, AZ, USA). After 10 days, cell counting kit-8 (CCK8) solution (Dojindo, Kumamoto, Japan) was employed to quantify cell viability. A microplate reader (ELX800, BioTek, Winooski, VT, USA) was employed to measure the 450 nm absorbance. Inhibitors with an inhibitory rate of more than 60% in 92-1 cells and less than 40% in PIG1 cells were selected. Further evaluation was performed with an eight-point 2-fold dilution series of seven selected inhibitors. Cell viability was evaluated after 10 days employing a CCK8 assay. The half-maximal inhibitory concentration (IC_{50}) was analyzed via Prism 8.0 software (GraphPad, San Diego, CA, USA). The selectivity index towards UM cells was calculated as follows: Selective index = IC_{50} (average in tumor cells)/IC_{50} (normal cells).

2.4. Immunofluorescence staining of human and mouse tissues

Deparaffinized tissues were rehydrated and fixed. Normal goat serum (5%) was used for blocking. Primary antibodies were incubated with the tissue at 4 °C overnight and secondary antibodies (4412, CST, Danvers, MA, USA, 1:1000) were incubated with the tissue for 1 h. 4′,6-diamidino-2-phenylindole (DAPI; Sigma-Aldrich, St. Louis, MO, USA) was employed to counterstain nuclei for 10 min. Images were acquired through an upright microscope (ZEISS Axio Scope A1, Oberkochen, Germany). The primary antibodies used in the assay were anti-DOT1L (ab64077, Abcam, Waltham, MA, USA, 1:200), anti-H3K79me2 (ab3594, Abcam, 1:500), and anti-NAPRT (13549-1-AP, Proteintech, Wuhan, China, 1:200).

2.5. Quantitative real-time polymerase chain reaction (PCR)

An RNA Purification Kit (EZBioscience, Roseville, MN, USA) was employed to extract total RNA from cells. Complementary DNA was produced by a PrimeScript RT Reagent Kit (Takara, Shiga, Japan). PCR Master Mix (SYBR Green, Life Technologies, Waltham, MA, USA) and a PCR system (Applied Biosystems, Irvine, CA, USA) were employed for the experiment. PCR products were quantified and normalized by β-actin (ACTB). The primers used in the study are listed in Table S1.

2.6. Western blotting analyses

Tissue and cell extracts supplemented with lysis buffer RIPA (BL504A, Biosharp, Hefei, China) were centrifuged for 30 min at 13,000 *g*. Samples were detached by 7.5% (*m*/*V*) sodium dodecyl sulfate polyacrylamide gel electrophoresis and then transferred to polyvinylidene fluoride membranes (Millipore, Billerica, MA, USA). The membranes were blocked with 5% milk for 1 h and incubated with primary antibody at 4 °C overnight and secondary antibodies (5151S and 5257S, CST, 1:30000) for 1 h. Bands were visualized with an Odyssey Infrared Imaging System (LI-COR, Lincoln, NE, USA). The primary antibodies were anti-DOT1L (ab64077, Abcam, 1:500), anti-H3K79me2 (ab3594, Abcam, 1:1000), anti-NAPRT (13549-1-AP, Proteintech, 1:2000), anti-Histone H3 (4499, CST, 1:2000), and anti-ACTB (3700, CST, 1:1000).

2.7. Plasmid construction, lentiviral packaging, and generation of stable cell lines

The pGMLV-SC5 and pGMLV-6395 vectors were used in our study. Short hairpin RNAs (shRNAs) and a negative control were generated through PCR and cloned into the pGMLV-SC5 vector. To overexpress NAPRT, the NAPRT sequence was generated through PCR, inserted into the pGMLV-6395 vector, and then verified by DNA sequencing. A total of 3 μg of shRNA plasmid, 3 μg of pMD2.G plasmid, and 6 μg of psPAX2 plasmid were transfected into

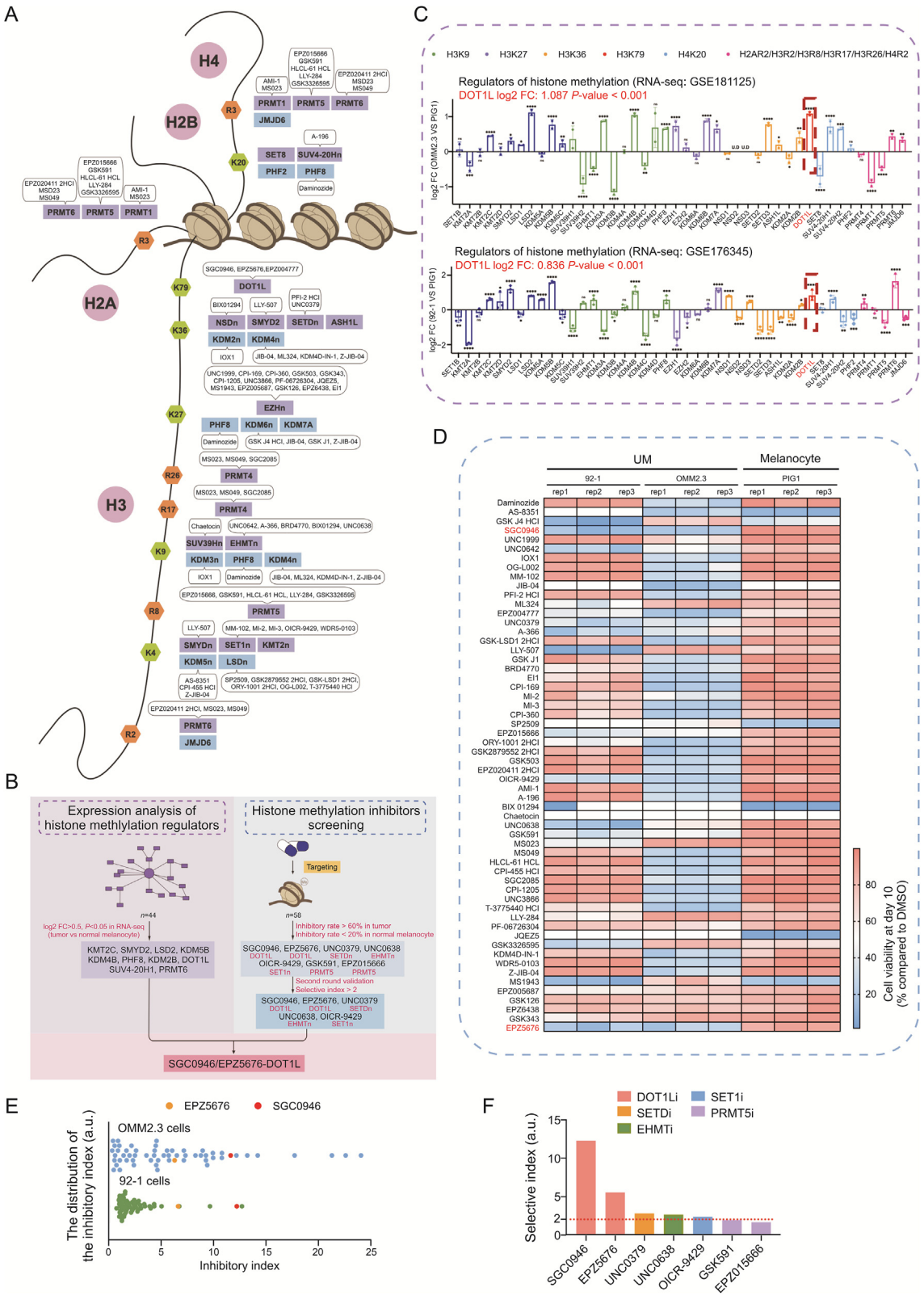

Fig. 1. Identification of disruptor of telomeric silencing 1-like (DOT1L) as a targetable histone modification regulator and the DOT1L inhibitors as effective inhibitors in uveal melanoma (UM). (A) Overview of histone methyltransferases (purple) and demethylases (blue). H2A: histone 2A; H2B: histone 2B; H3: histone 3; H4: histone 4; K4: lysine 4; K9: lysine 9; K20: lysine 20; K27: lysine 27; K36: lysine 36; K79: lysine 79; R2: arginine 2; R3: arginine 3; R8: arginine 8; R17: arginine 17; R26: arginine 26; SET1B: SET domain containing 1B; KMT2A: lysine methyltransferase 2A; KMT2B: lysine methyltransferase 2B; KMT2C: lysine methyltransferase 2C; KMT2D: lysine methyltransferase 2D; SMYD2: SET and MYND domain containing 2; LSD1: lysine demethylase 1A; LSD2: lysine demethylase 1B; KDM5A: lysine demethylase 5A; KDM5B: lysine demethylase 5B; KDM5C: lysine demethylase 5C; SUV39H1: suppressor of variegation 3–9 homolog 1; SUV39H2: suppressor of variegation 3–9 homolog 2; EHMT1: euchromatic histone lysine methyltransferase 1; KDM3A: lysine demethylase 3A; KDM3B: lysine demethylase 3B; KDM4A: lysine demethylase 4A; KDM4B: lysine demethylase 4B; KDM4C: lysine demethylase 4C; KDM4D: lysine demethylase 4D; PHF8: PHD finger protein 8; EZH2: enhancer of zeste 2 polycomb repressive complex 2 subunit; KDM6A: lysine demethylase 6A; KDM6B: lysine

HEK239T cells by Lipofectamine 2000 (Invitrogen, Carlsbad, CA, USA) in reduced serum OptiMEM I (Gibco). The original medium was substituted with complete medium 6 h after transfection. After 48 and 72 h of transfection, the virus-containing supernatant was acquired, filtered through a 0.45-mm filter from Millipore, and concentrated through a Takara Lenti-X concentrator. A total of 25 μL/mL concentrated lentivirus mixed with 8 ng/mL polybrene (Sigma-Aldrich) was added to cell medium and maintained for 48 h. Puromycin (InvivoGen, San Diego, CA, USA) was employed to select stable cell lines at 4 μg/mL for 2 weeks and maintained at 1 μg/mL.

2.8. Cell proliferation

CCK8 assays were utilized to evaluate cell proliferation capability. Cells were cultured in Corning 96-well plates at 1000–2000 cells per well. A solution of 10 μL of Dojindo CCK8 was added to each well. A microplate reader (ELX800, BioTek) was employed to measure 450 nm absorbance. Moreover, colony formation assays were applied to assess cell proliferation. Medium containing 1000 cells was added to a 6-well plate and cultured for 7–14 days. Then, the medium was removed and 0.25% crystal violet was employed to stain the colonies.

2.9. Apoptosis assay

Apoptosis assays were implemented by a FITC-Annexin V Apoptosis Detection Kit 1 (BD Biosciences, San Diego, CA, USA). Cells were washed using phosphate buffer sodium (PBS; Gibco), stained with propidium iodide (PI) and FITC-Annexin V for 5 min, and then subjected to flow cytometric analysis with a BD LSRFortessa analyzer.

2.10. Cell cycle analysis

Cells were washed using PBS (Gibco), fixed with precooled 75% ethanol overnight at 4 °C, treated with RNase A (Qiagen, Hilden, Germany) at 37 °C for 30 min, and stained with 50 μL/mL PI. The prepared cells were analyzed using a BD LSRFortessa analyzer.

2.11. Orthotopic xenograft models

Male BALB/c nude mice (4 weeks old) were intraperitoneally anesthetized by employing a ketamine (10 mg/mL)/xylazine (1 mg/mL) combination (0.01 mL/g weight). A 30-gauge injection needle was employed to pre-perforate the sclera, and 5×10^6 OMM2.3 cells pretreated for 10 days with 10 μM SGC0946 or dimethyl sulfoxide (DMSO) were then injected with a 33-gauge microinjection needle (7803-05, Hamilton, Reno, NV, USA) into the perforation in the choroid. The experiments were performed in a specific pathogen-free room. Bioluminescence was measured after 28 days with an in vivo animal imaging system. The tumors were fixed with 4% formaldehyde, embedded in paraffin, and stained with hematoxylin and eosin. The study was approved by the Animal Care and Use Committee of Shanghai Jiao Tong University School of Medicine.

2.12. Cleavage Under Targets and Tagmentation (CUT&Tag)

The experiment was completed as previous description with alterations [14]. In brief, 1×10^5 cells were washed twice using wash buffer (1× protease inhibitor cocktail, 20 mM HEPES, 0.5 mM spermidine and 150 mM NaCl). A volume of 10 μL of concanavalin A-coated magnetic beads (Bangs Laboratories, Inc., Fishers, IN, USA) was added to each sample and then incubated for 10 min. The unbound supernatant and resuspended cells were removed with dig wash buffer (0.5 mM spermidine, 20 mM HEPES, 150 mM NaCl, 2 mM ethylenediamine tetraacetic acid, 0.05% digitonin, and 1× protease inhibitor cocktail). The cells were incubated with an anti-H3K79me2 antibody (ab3594, Abcam, 1:50) or IgG antibody (12–370, Millipore) on a rotating platform for 2 h at room temperature (RT) or overnight at 4 °C. The cells were incubated first with a secondary antibody (AP132, Millipore, 1:100) for 60 min at RT, subsequently with pA-Tn5 adapter complex (1:100) at RT for 60 min and with tagmentation buffer (10 mM $MgCl_2$ in dig-med buffer) for 60 min at 37 °C. DNA was extracted by phenol-chloroform-isoamyl alcohol and precipitated by ethanol. For library amplification, 21 μL of DNA was integrated with 2 μL of i5 and i7 primers. The mixture was added to 25 μL of NEBNext HiFi 2 × PCR Master Mix, transferred in a thermocycler, and subjected to the cycling conditions: 72 °C for 5 min (gap filling); 98 °C for 30 s; 14 cycles of 98 °C for 10 s and 63 °C for 30 s; 72 °C for 1 min (final extension); and holding at 8 °C. An Illumina NovaSeq 6000 system (San Diego, CA, USA) was used for sequencing by 150-bp paired-end sequencing. The criteria of fold change >2.0 (log2 ratio value > 1) and P value < 0.05 were employed to identify differentially accessible peaks.

2.13. Chromatin immunoprecipitation (ChIP)

A total of 1×10^9 cells were fixed with 1% formaldehyde and then sonicated 10 times on and 15 times off using a 2-mm microtip for 8 min. A dilution of 1:10 sonicated chromatin fragments (150 μL) and Protein G agarose (Millipore) was mixed and incubated for 2 h. Next, the sample was centrifuged at 1,000 rpm for 5 min. Anti-H3K79me2 (ab3594, Abcam) or anti-DOT1L (ab64077, Abcam) antibodies were supplemented and incubated at 4 °C overnight. The proteins were pulled down through 60 μL of Protein A and Protein G magnetic beads (Millipore). DNA was acquired from the bound chromatin. The precipitated DNA was diluted in 100 μL of 0.2 M glycine following

demethylase 6B; KDM7A: lysine demethylase 7A; NSD1: nuclear receptor binding SET domain protein 1; NSD2: nuclear receptor binding SET domain protein 2; NSD3: nuclear receptor binding SET domain protein 3; SETD2: SET domain containing 2; ASH1L: ASH1 like histone lysine methyltransferase; KDM2A: lysine demethylase 2A; KDM2B: lysine demethylase 2B; DOT1L: disruptor of telomeric silencing 1-like; SET8: SET domain-containing protein 8; SUV4–20H1: Suppressor of variegation 4–20 homolog 1; SUV4–20H2: Suppressor of variegation 4–20 homolog 2; PHF2: PHD finger protein 2; PRMT4: protein arginine methyltransferase 4; PRMT1: protein arginine methyltransferase 1; PRMT5: protein arginine methyltransferase 5; PRMT6: protein arginine methyltransferase 6; JMJD6: jumonji domain containing 6. (B) Schematic diagram of the expression analysis and drug screening procedures. Inhibitory rate (%) = 1−Cell viability (%). Selective index = IC_{50} (average in tumor cells)/IC_{50} (normal melanocytes). (C) Histograms comparing the expression of histone methylation regulators between UM cell lines (OMM2.3 and 92-1) and a normal melanocyte cell line (PIG1). The data are presented as the means ± standard deviation of biological duplicates for OMM2.3 and PIG1 cells and biological triplicates for 92-1 and PIG1 cells. Significance was determined by unpaired two-tailed Student's t-test. $^{*}P < 0.05$, $^{**}P < 0.01$, $^{***}P < 0.001$, $^{****}P < 0.0001$, ns: no significance, U.D: undected. (D) Heatmap of histone methylation inhibitor screening results in UM cell lines (OMM2.3 and 92-1) and a normal melanocyte cell line (PIG1) upon treatment with dimethyl sulfoxide (DMSO) or inhibitors (10 μM) for 10 days. Data are presented over biological triplicates. (E) The distribution of the inhibitory index in OMM2.3 and 92-1 cells relative to PIG1 cells upon treatment with DMSO or inhibitors (10 μM) for 10 days. The blue dots mean the inhibitory index of histone methylation inhibitors in OMM2.3 cells and the green dots mean the inhibitory index of histone methylation inhibitors in 92-1 cells. Inhibitory index = Inhibitory rate (tumor cells)/Inhibitory rate (normal melanocytes). Inhibitory rate (%) = 1−Cell viability (%). (F) Selective indices of the 7 histone methylation inhibitor candidates for UM cells. Each of these seven inhibitors exhibited an inhibitory rate greater than 60% in 92-1 cells and less than 20% in PIG1 cells. Selective index = IC_{50} (average in tumor cells)/IC_{50} (normal melanocytes), Inhibitory rate (%) = 1−Cell viability (%). Specific IC_{50} values of the 7 inhibitors are shown in Fig. S1D. DOT1Li: DOT1L inhibitor; SETDi: SETDn inhibitor; EHMTi: EHMTn inhibitor; SET1i: SET1n inhibitor; PRMT5i: PRMT5 inhibitor.

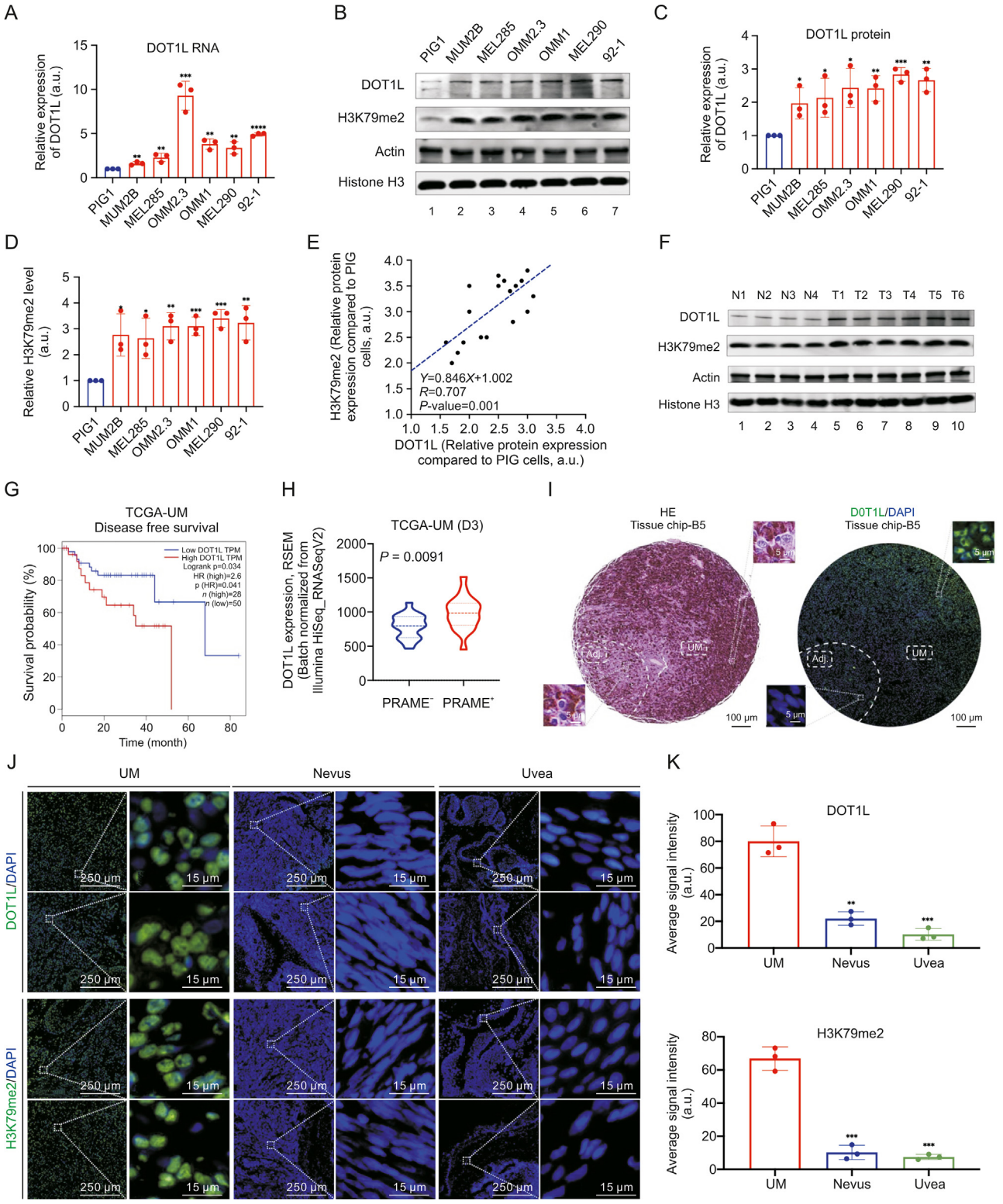

Fig. 2. Uveal melanoma (UM) exhibited increased disruptor of telomeric silencing 1-like (DOT1L) expression and dimethylation of histone H3 lysine 79 (H3K79me2) levels, which were associated with poor survival in UM patients. (A) Real-time polymerase chain reaction data showing the DOT1L expression in UM cells relative to PIG1 cells. The data are presented as the mean ± standard deviation (SD) of experimental triplicates. Significance was determined by unpaired two-tailed Student's *t*-test. $^{**}P < 0.01$, $^{***}P < 0.001$, $^{****}P < 0.0001$. (B) Western blotting of DOT1L and H3K79me2 relative to β-actin (ACTB) and histone H3, respectively, in UM cells and normal melanocytes. The data are representative of experimental triplicates. (C, D) Densitometric analysis showing the protein expression of DOT1L relative to ACTB (C) and the level of H3K79me2 relative to histone H3 (D) in UM cells and normal melanocytes. The data are presented as the mean ± SD of experimental triplicates. Significance was determined by unpaired two-tailed Student's *t*-test. $^{*}P < 0.05$, $^{**}P < 0.01$, $^{***}P < 0.001$. (E) Correlation analysis of relative protein expression between DOT1L protein expression and H3K79me2 level in UM cells and normal melanocytes. Significance was determined by *Pearson* correlation analysis ($R = 0.707$, $P = 0.001$). (F) Western blotting of DOT1L and H3K79me2 relative to ACTB and histone H3, respectively, in clinical tumor samples and normal samples. (G) Kaplan-Meier analysis showing the correlations between DOT1L expression and disease-free survival in the Cancer Genome Atlas (TCGA)-UM patients stratified by the DOT1L expression level: high (top 36th percentile, $n = 28$) or low (bottom 64th percentile, $n = 50$). Significance was determined by a two-sided

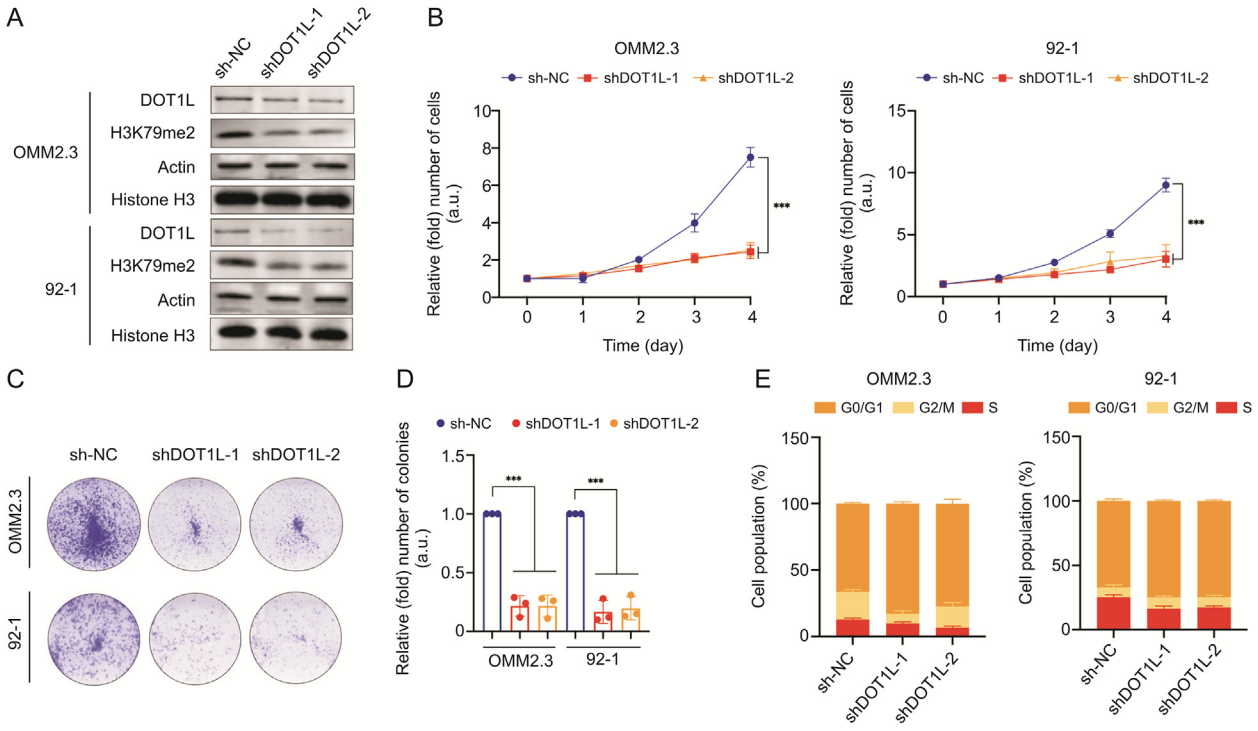

Fig. 3. Disruptor of telomeric silencing 1-like (DOT1L) knockdown decreased the dimethylation of histone H3 lysine 79 (H3K79me2) levels and suppressed uveal melanoma (UM) tumorigenesis. (A) Western blotting of DOT1L and H3K79me2 relative to β-actin (ACTB) and histone H3, respectively, in UM cells (OMM2.3 and 92-1) upon DOT1L knockdown. (B) A cell counting kit-8 (CCK8) assay was performed to assess the proliferation of UM cells (OMM2.3 and 92-1) upon DOT1L knockdown. The data are presented as the mean ± standard deviation (SD) of experimental triplicates. Significance was determined by unpaired two-tailed Student's *t*-test. $^{***}P < 0.001$. (C) A colony formation assay was performed to assess the growth of UM cells (OMM2.3 and 92-1) upon DOT1L knockdown. Representative images from three experimental replicates are shown. (D) Statistical analysis of the colony formation assay data in UM cells (OMM2.3 and 92-1) upon DOT1L knockdown. The data are presented as the mean ± SD of experimental triplicates. Significance was determined by unpaired two-tailed Student's *t*-test. $^{***}P < 0.001$. (E) Cell cycle phases distribution in UM cells (OMM2.3 and 92-1) upon DOT1L knockdown. The data are presented as the mean ± SD of experimental triplicates. Significance was determined by unpaired two-tailed Student's *t*-test. Specific data from the cell cycle analysis are provided in Fig. S2C.

cross-linking reversal and proteinase K treatment. The primers used in the study are listed in Table S1.

2.14. RNA sequencing (RNA-seq)

TRIzol Reagent (Invitrogen, Carlsbad, CA, USA) was employed to extract total RNA. The integrity was confirmed using a 2100 Bioanalyzer (Agilent Technologies, Beijing, China). The concentration was measured by a Qubit 2.0 fluorometer (Life Technologies, Carlsbad, CA, USA). The library was established from 100 ng of RNA through an Illumina TruSeq RNA Sample Prep Kit and then sequenced on the Illumina HiSeq 2500 platform. TopHat v2.0.9 was used to identify the mRNA levels. The DESeq2 algorithm was performed to filter the differentially expressed genes. The criteria of fold change <0.5 or >2.0 (log2 ratio value <− 1 or >1) and *P* value < 0.05 were employed to identify differentially expressed genes.

2.15. NAD^+ measurement

Cells of 2 × 10^6 for each sample were harvested through scraping, washed in PBS (Gibco), and suspended in a tube by spinning at 2,000 rpm for 5 min. NAD^+ was measured by the NAD^+/NADH kit (ab65348, Abcam). Colorimetric measurements were completed at 450 nm absorbance through a microplate reader (ELX800, BioTek).

2.16. The Cancer Genome Atlas (TCGA) dataset

To explore the prognosis of DOT1L and NAPRT, and identify correlations in their expression in UM, we queried the Gene Expression Profiling Interactive Analysis website (gepia.cancerpku.cn) to acquire the transcriptional landscape and survival analysis corresponding to UM samples.

2.17. Statistical analyses

The mean ± standard deviation values were employed to describe the data. The differences between two groups were analyzed through an unpaired Student's *t*-test in GraphPad Prism 8.0 software. Kaplan-Meier and log-rank tests were performed for survival analysis. $P < 0.05$ was considered statistically significant. Asterisks represent statistical significance ($^*P < 0.05$, $^{**}P < 0.01$, $^{***}P < 0.001$, and $^{****}P < 0.0001$).

log-rank test. (H) Comparison of DOT1L expression between the groups with high preferentially expressed antigen in melanoma (PRAME) expression ($n = 19$) and with low PRAME expression ($n = 19$) in TCGA-UM cohort of disomy 3 (D3) ($n = 38$). The violin plot shows the interquartile ranges (lines) and the observed number (width). Significance was determined by unpaired two-tailed Student's *t*-test. (I) Immunofluorescence of DOT1L (green) and 4',6-diamidino-2-phenylindole (DAPI) (blue) in UM. Hematoxylin and eosin (HE) staining was performed to visualize UM tissues and adjacent tissues (Adj.). (J) Immunofluorescence of DOT1L, H3K79me2 (green) and 4',6-diamidino-2-phenylindole (DAPI) (blue) in UM samples and normal samples (nevus and uvea tissues). Representative images from three biological specimens are shown. (K) Statistical histogram of the DOT1L and H3K79me2 immunofluorescence staining data in UM samples and normal samples (nevus and uvea tissue). The data are presented as the mean ± SD of biological triplicates. Significance was determined by unpaired two-tailed Student's *t*-test. $^{**}P < 0.01$, $^{***}P < 0.001$.

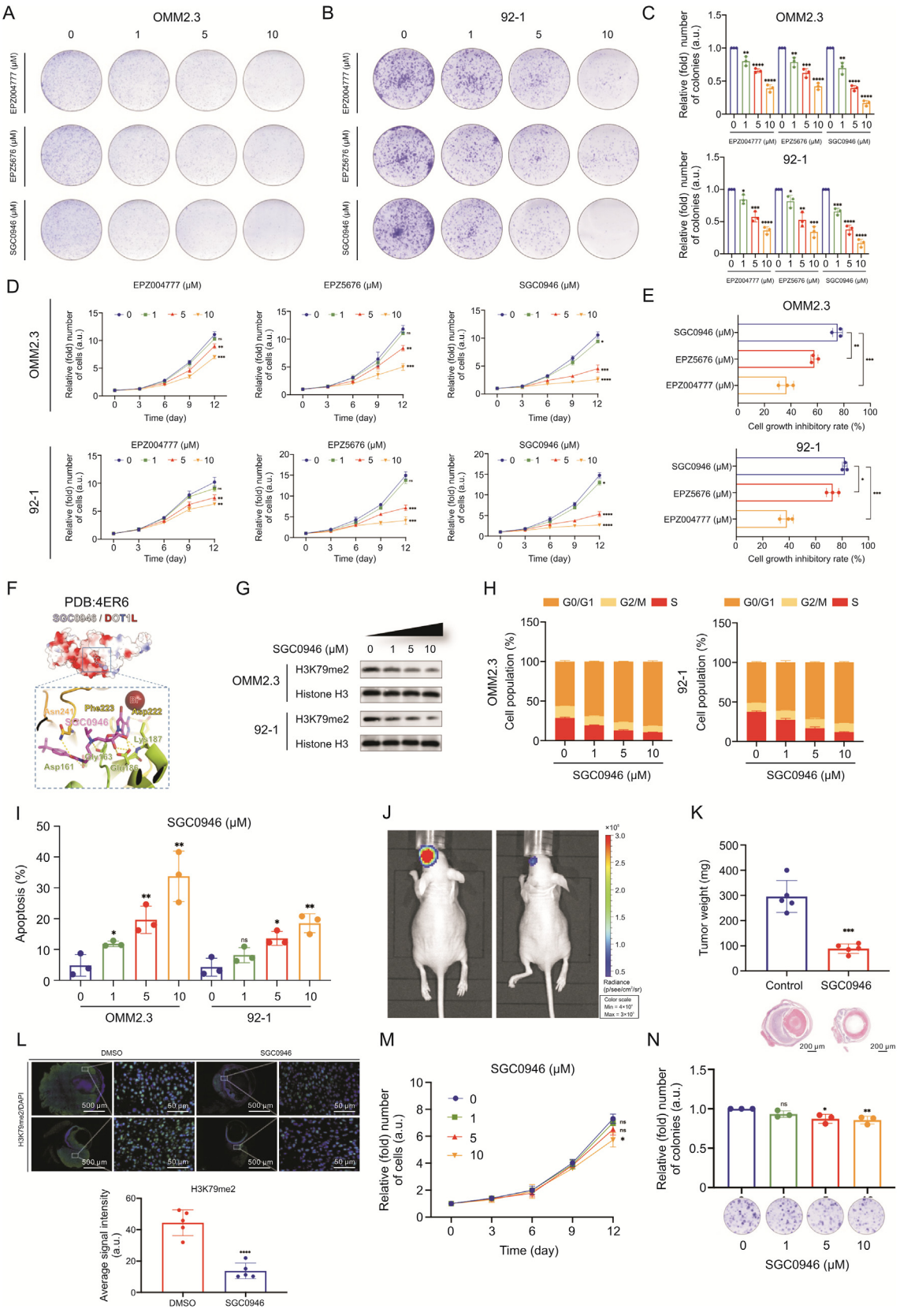

Fig. 4. Disruptor of telomeric silencing 1-like (DOT1L) inhibitor treatment reduced the dimethylation of histone H3 lysine 79 (H3K79me2) levels and suppressed uveal melanoma (UM) growth. (A, B) A colony formation assay was performed to assess the growth of OMM2.3 (A) and 92-1 (B) cells upon treatment with different concentrations of EPZ004777, EPZ5676 or SGC0946. Representative images from three experimental replicates are shown. (C) Statistical analysis of the colony formation assay data in UM cells (OMM2.3 and 92-1) upon treatment with different concentrations of EPZ004777, EPZ5676 or SGC0946. The data are presented as the mean ± standard deviation (SD) of experimental triplicates. Significance was determined by unpaired two-tailed Student's *t*-test. $^{*}P < 0.05$, $^{**}P < 0.01$, $^{***}P < 0.001$, $^{****}P < 0.0001$. (D) A cell counting kit-8 (CCK8) assay was performed to assess

3. Results

3.1. H3K79 methyltransferase DOT1L served as a druggable target in UM

To explore the pattern of histone methylation in UM, we have listed all histone methyltransferases (Fig. 1A, purple) and demethylases (Fig. 1A, blue) with their targeted inhibitors. Subsequently, we have presented a histone methylation drug screening and compared the expression levels of involved targets between UM and normal melanocyte control (Fig. 1B). RNA-seq (GSE181125 and GSE176345) between two UM cell lines (OMM2.3 and 92-1) and a normal melanocyte cell line (PIG1) was performed (Figs. S1A and B). OMM2.3 and 92-1 are representative UM cell lines and have been widely used in UM research [15,16], while PIG1 is a commonly used normal melanocyte control [17,18]. Two biological replicates were used for OMM2.3 and PIG1 cells and three biological replicates were used for 92-1 and PIG1 cells. The RNA-seq data revealed ten histone modifiers were identified with an increased expression in both two UM cell lines, including lysine methyltransferase 2C, SET and MYND domain containing 2, lysine demethylase 1B, lysine demethylase 5B, lysine demethylase 4B, PHD finger protein 8, lysine demethylase 2B, DOT1L, suppressor of variegation 4–20 homolog 1, and protein arginine methyltransferase 6 (Fig. 1C). The drug screening revealed that five inhibitors exhibited sufficient selective inhibition efficacy in UM after two rounds of validation, namely, SGC0946 (DOT1L inhibitor), EPZ5676 (DOT1L inhibitor), UNC0379 (inhibitor of SET domain containing), UNC0638 (inhibitor of euchromatic histone lysine methyltransferase), and OICR-9429 (inhibitor of SET domain containing 1) (Figs. 1D–F and S1C–E). Taken together, these data aggregated the fact that UM cells presented with an enriched expression of H3K79 methyltransferase DOT1L, conferring vulnerability towards its inhibitors (EPZ5676 and SGC0946).

3.2. DOT1L mediated H3K79 methylation was specifically enriched in UM

We subsequently examined DOT1L expression and H3K79 methylation levels in both UM cells and clinical samples. Real-time PCR and Western blotting analysis exhibited an enhanced DOT1L expression with an increased H3K79me2 level in most UM cell lines (MUM2B, MEL285, OMM2.3, OMM1, MEL290, and 92-1) (Figs. 2A–D). Notably, correlation analysis further demonstrated the significantly correlated expressions of DOT1L and H3K79me2 ($R = 0.707$, $P < 0.05$, Fig. 2E). Western blotting analysis showed that H3K79me2 and DOT1L levels were increased in clinical UM samples compared with normal uvea samples (Fig. 2F, and Table S2). Nevertheless, DOT1L upregulation was associated with unfavorable disease-free survival (log-rank, $P = 0.034$) in TCGA-UM cohort (Fig. 2G). Importantly, preferentially expressed antigen in melanoma (PRAME) is an independent prognostic biomarker, referring to an enhanced metastatic risk in UM [9,19,20]. Notably, increased DOT1L expression was noted in the UM patients with an elevated risk of metastasis ($PRAME^{+}$) in TCGA-UM cohort (Fig. 2H). Immunofluorescence staining of UM samples indicated an enhanced expression of DOT1L in tumor tissues compared to the expression in tumor adjacent tissues (Fig. 2I). Furthermore, compared with nevus and uvea tissues, UM tissues exhibited upregulated DOT1L expression and H3K79me2 levels (Figs. 2J, 2K and S2A). These data indicated that H3K79me2 and its methyltransferase DOT1L were tumor-specifically elevated, serving as a potential diagnostic/prognostic marker in UM.

3.3. Inhibition of DOT1L attenuated UM both in vitro and in vivo

To evaluate whether DOT1L inhibition attenuates tumorigenesis in UM, we first reduced the DOT1L expression level by transfecting two shRNAs into these cells (Figs. 3A and S2B). Correspondingly, DOT1L-deficient UM cells exhibited a marked reduction in H3K79me2 (Fig. 3A). In addition, shRNA-mediated DOT1L knockdown suppressed growth (Fig. 3B) and colony formation (Figs. 3C and D) of UM cells and induced G1/S arrest (Figs. 3E and S2C). Furthermore, we treated UM cells (OMM2.3 and 92-1 cells) with three individual DOT1L inhibitors (EPZ004777, EPZ5676, and SGC0946). Similarly, DOT1L inhibitors triggered a significant dose-dependent suppression in UM cells, including decreased colony formation capacity (Figs. 4A–C) as well as delayed cellular proliferation (Fig. 4D). SGC0946 exhibited a more efficient inhibitory efficacy compared to the other two inhibitors (Fig. 4E). The interface between SGC0946 and DOT1L active pocket underscored the inhibitory role of SGC0946 (Fig. 4F). Notably, a significant dose-dependent decrease in H3K79me2 levels after SGC0946 treatment was observed in UM cells, indicating an on-target effect of SGC0946 in the abrogation of H3K79 dimethylation (Fig. 4G). In addition, SGC0946 induced G1/S arrest (Figs. 4H and S3A) and apoptosis (Figs. 4I and S3B) in all tested UM cells. For in vivo analysis, we injected OMM2.3 cells pretreated for 10 days with

the proliferation of UM cells (OMM2.3 and 92-1) upon treatment with different concentrations of EPZ004777, EPZ5676 or SGC0946. The data are presented as the mean ± SD of experimental triplicates. Significance was determined by unpaired two-tailed Student's *t*-test. $^{*}P < 0.05$, $^{**}P < 0.01$, $^{***}P < 0.001$, $^{****}P < 0.0001$. (E) Statistical analysis of the cell growth inhibitory rate based on the CCK8 assay after treatment with 10 μM EPZ004777, EPZ5676 or SGC0946 for 12 days. The data are presented as the mean ± SD of experimental triplicates. Significance was determined by unpaired two-tailed Student's *t*-test. $^{*}P < 0.05$, $^{**}P < 0.01$, $^{***}P < 0.001$. Inhibitory rate (%) = 1−Cell viability (12 day, %)/Cell viability (0 day, %). (F) Top: Electric potential of SGC0946/DOT1L complex (Positive charge: red, negative charge: blue). Bottom: A close-up atomic model of SGC0946/DOT1L interface. This figure was modified from Yu et al. [34]. (G) Western blotting of H3K79me2 relative to histone H3 in OMM2.3 and 92-1 cells upon treatment with different concentrations of SGC0946 for 10 days. (H) Cell cycle phase distribution in UM cells (OMM2.3 and 92-1) upon treatment with different concentrations of SGC0946 for 10 days. The data are presented as the mean ± SD of biological triplicates. Significance was determined by unpaired two-tailed Student's *t*-test. Specific data from the cell cycle analysis are provided in Fig. S3A. (I) Apoptosis level in UM cells (OMM2.3 and 92-1) upon treatment with different concentrations of SGC0946 for 10 days. The data are presented as the mean ± SD of biological triplicates. Significance was determined by unpaired two-tailed Student's *t*-test. $^{*}P < 0.05$, $^{**}P < 0.01$. Specific data from the apoptosis assay are provided in Fig. S3B. (J) Images acquired with an in vivo small animal imaging system showing the suppression of bioluminescent signals in orthotopic xenografts derived from pretreated OMM2.3 cells (10 μM SGC0946 for 10 days). Representative images from five biological replicates are shown. The remaining images are provided in Fig. S4. (K) Histograms of the weights of orthotopic xenografts derived from pretreated OMM2.3 cells (10 μM SGC0946 for 10 days). Hematoxylin and eosin staining was performed to visualize tumor tissues. Representative images from five biological replicates are shown. The data are presented as the mean ± SD values. Significance was determined by unpaired two-tailed Student's *t*-test. $^{***}P < 0.001$. (L) Immunofluorescence of H3K79me2 (green) and 4',6-diamidino-2-phenylindole (DAPI) (blue) in orthotopic xenografts. Statistical histogram of the H3K79me2 immunofluorescence staining data in dimethyl sulfoxide (DMSO) and SGC0946-treated groups. The data are presented as the means ± SD of biological triplicates. Significance was determined by unpaired two-tailed Student's *t*-test. $^{****}P < 0.0001$. (M) A CCK8 assay was performed to assess the proliferation of normal melanocytes (PIG1) upon treatment with different concentrations of SGC0946. The data are presented as the mean ± SD of experimental triplicates. Significance was determined by unpaired two-tailed Student's *t*-test. $^{*}P < 0.05$, ns: no significance. (N) A colony formation assay was performed to assess the growth of normal melanocytes (PIG1) upon treatment with different concentrations of SGC0946. Representative images from three experimental replicates are shown. The data are presented as the mean ± SD values. Significance was determined by unpaired two-tailed Student's *t*-test. $^{*}P < 0.05$, $^{**}P < 0.01$, ns: no significance.

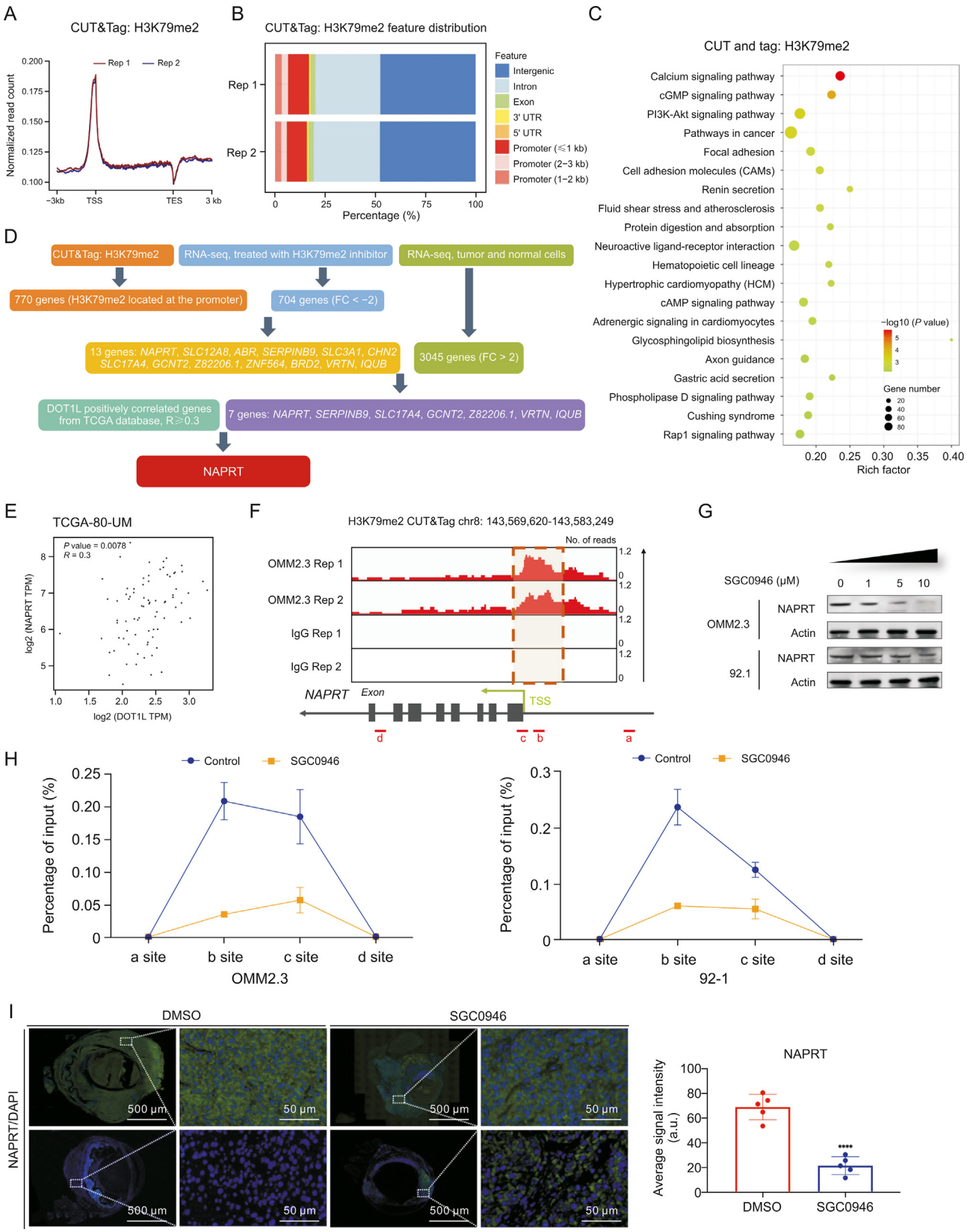

Fig. 5. Dimethylation of histone H3 lysine 79 (H3K79me2) activated the transcription of nicotinate phosphoribosyltransferase (NAPRT). (A) Cleavage Under Targets and Tagmentation (CUT&Tag) data showing the distribution of H3K79me2 sites relative to the translation start site. Biological duplicates were analyzed. TSS: transcription start site; TES: transcription end site. (B) Abundance of H3K79me2 feature distribution. Biological duplicates were analyzed. (C) Kyoto Encyclopedia of Genes and Genomes analysis showing the top pathways enriched with H3K79me2-specific genes in uveal melanoma (UM) cells (OMM2.3). Biological duplicates were analyzed. (D) Bioinformatics analysis identifying NAPRT as a downstream target of H3K79me2. SLC12A8: solute carrier family 12 member 8; ABR: ABR activator of RhoGEF and GTPase; SERPINB9: serpin family B member 9; SLC3A1: solute carrier family 3 member 1; CHN2: chimerin 2; SLC17A4: solute carrier family 17 member 4; GCNT2: glucosaminyl (N-acetyl) transferase 2; ZNF564: zinc finger protein 564; BRD2:

10 μM SGC0946 or DMSO to establish the orthotopic model. After 28 days, we observed that DOT1L inhibition significantly attenuated the growth of UM in the orthotopic model (Figs. 4J, 4K, and S4), following the reduction in the H3K79me2 in the SGC0946-treated group (Fig. 4L). In contrast, although SGC0946 had an effect on the growth behaviors of normal melanocytes (PIG1) at 5 and 10 μM (Figs. 4M and N), the effect was less obvious than that in UM cells (OMM2.3 and 92-1 cells) (Figs. 4A–D), indicating a tumor-specific cytotoxic effect.

3.4. NAPRT served as the downstream target of DOT1L

To reveal the function of DOT1L in the transcriptional regulation of UM, we presented CUT&Tag using anti-H3K79me2 antibodies in the OMM2.3 cell line (GSE181121) and RNA-seq in OMM2.3 cells upon SGC0946 treatment (GSE181125). For the CUT&Tag assay, OMM2.3 cells bound with magnetic beads were incubated with an anti-H3K79me2 antibody or IgG control antibody and then incubated with a secondary antibody and subsequent pA-Tn5 adapter complex. DNA was purified and amplified for library establishment. After sequencing, the criteria of fold change > 2.0 and P value < 0.05 were employed to identify differentially accessible peaks. For RNA-seq, RNA was extracted from OMM2.3 cells with or without SGC0946 treatment. We confirmed the integrity, measured the concentration, prepared and sequenced the libraries. The differentially expressed genes were filtered by the DESeq2 algorithm and identified under the criteria of fold change < 0.5 or > 2.0 and P value < 0.05.

The CUT&Tag data revealed that H3K79me2 was enriched in the near translation start site region, which agreed with its function as a transcriptional activator in the promoter [21] (Figs. 5A, 5B, S5A, and S5B). Kyoto Encyclopedia of Genes and Genomes analysis suggested that H3K79me2-enriched pathways were associated with tumorigenesis, including PI3K–Akt pathway, pathways in cancer, and Rap1 signaling pathway (Fig. 5C). According to our RNA-seq data (GSE181125, Table S3), we observed 57 down-regulated genes, which participated in several oncogenesis-related pathways, including the ECM-receptor pathway and pathways in cancer (Fig. S5C). In addition, 45 genes were upregulated after applying SGC0946 in UM cells, and these genes were enriched in T cell differentiation, apoptosis and Notch signaling pathways (Fig. S5D). These high-throughput sequencing data revealed that both DOT1L inhibition and H3K79 methylation pattern were associated with the malignant transformation in UM cells, which agreed with the tumor inhibitory effect of SGC0946.

Combining CUT&Tag data (orange), the transcriptome data after using SGC0946 (blue), and the expression data of UM cells (green) (GSE181125), we found that seven genes met the following criteria: 1) presented with an H3K79me2 modified promoter; 2) presented with a decreased expression after treating SGC0946; and 3) elevated expression in UM cells (Fig. 5D). Herein, we identified an important enzyme in the biosynthesis of NAD^+, NAPRT [22], which was positively correlated with DOT1L in TCGA-UM cohort (Fig. 5E, $R = 0.3$, $P < 0.01$). The chromatogram of CUT&Tag reads revealed that *NAPRT* contained an H3K79me2 peak in its promoter (Fig. 5F). Furthermore, we observed a dose-dependent reduction in NAPRT expression in tumor cells treated with SGC0946, as was revealed by real-time PCR and Western blotting (Figs. 5G and S6A). Consistently, the mRNA and protein levels of NAPRT were significantly decreased after silencing DOT1L (Figs. S6B and C). Importantly, ChIP-qPCR assays demonstrated that H3K79me2 was significantly decreased at *NAPRT* promoter regions with SGC0946 treatment (Fig. 5H). Notably, only a slight decrease was observed in the DOT1L binding signal after treatment with SGC0946 (Figs. S7A and B). The decrease of DOT1L binding of *NAPRT* might be attributed to the conformation change of DOT1L inhibitors [23], which further prevented efficient recognition of histone tails and thereby attenuated the histone binding of DOT1L. Moreover, in the in vivo model, we also discovered a parallel decrease in NAPRT expression following the decrease in H3K79 methylation after DOT1L inhibition (Fig. 5I). Taken together, these data suggest that NAPRT was activated by DOT1L by H3K79 methylation reprogramming in its promoter.

3.5. NAPRT acted as a novel oncogene in UM by modulating intracellular NAD^+ synthesis

We were then interested in exploring the oncogenic function of *NAPRT* in UM. First, TCGA-UM patients were investigated and revealed that high level of NAPRT in UM patients was associated with unfavorable overall survival and disease-free survival (log-rank, $P < 0.01$) compared to a low level of NAPRT in UM patients. More importantly, a high level of NAPRT was noted in TCGA-UM patients with a high risk of metastasis in D3 UM patients (Figs. 6A–C). Correlation analysis revealed significantly correlated expressions of NAPRT and DOT1L in D3 UM patients in TCGA cohort ($R = 0.5188$, $P = 0.0008$, Fig. 6D). Similarly, structural amplification of *NAPRT* was associated with a worse overall survival and disease-specific survival (Figs. S8A and B). Taken together, these bioinformatic data suggested that NAPRT functioned as an oncogenic accelerator.

We next evaluated the expression of NAPRT in UM tissues and cells. Immunofluorescence staining of tumor tissues suggested enhanced expression of NAPRT in UM compared with that of nevus or uvea tissues (Fig. 6E). RNA-seq, real-time PCR and Western blotting analysis suggested that NAPRT was highly expressed in UM cell lines (Figs. 6F–H, S8C and D). We determined the function of NAPRT in UM through silencing its expression using two shRNAs in UM cells (Figs. 6I and J). The level of H3K79me2 and the protein expression level of DOT1L were unchanged in NAPRT knockdown cells, confirming that NAPRT served as the downstream effector of DOT1L (Fig. 6J). Notably, significant inhibition of tumor cell growth (Fig. 6K) and tumor cell colony formation (Figs. 6L and M), along with G1/S arrest (Figs. 6N and S9), was observed in NAPRT-silenced cells. Together, the data indicated that NAPRT served as an oncogene in UM.

Since NAD^+ serves as an onco-metabolite that fuels various fundamental events during cancer development, including DNA repair, transcription, apoptosis, cell cycle progression, and metabolism [22], we evaluated the intracellular NAD^+ level in NAPRT

bromodomain containing 2; VRTN: vertebrae development associated; IQUB: IQ motif and ubiquitin domain containing; FC: fold change. (E) Correlation analysis of DOT1L expression and NAPRT expression in the Cancer Genome Atlas (TCGA)-UM cohort ($n = 80$). TPM: transcripts per million. Significance was determined by *Pearson* correlation analysis ($R = 0.3$, $P = 0.0078$). (F) Integrative Genomics Viewer tracks from CUT&Tag analysis showing H3K79me2 enrichment at the promoter of *NAPRT*. Sites a–d are distributed in the *NAPRT* genomic region, and sites b and c are the H3K79me2 peaks. Biological duplicates were analyzed. (G) Western blotting of NAPRT relative to β-actin (ACTB) in OMM2.3 and 92-1 cells upon treatment with different concentrations of SGC0946 for 10 days. (H) Chromatin immunoprecipitation (ChIP)-qPCR assay of H3K79me2 status in the *NAPRT* genomic region in UM cells (OMM2.3 and 92-1) upon treatment with dimethyl sulfoxide (DMSO) or 10 μM SGC0946 for 10 days. The data are presented as the mean ± standard deviation (SD) of experimental triplicates. (I) Immunofluorescence of NAPRT (green) and DAPI (blue) in orthotopic xenografts. Statistical histogram of the NAPRT immunofluorescence staining data in DMSO and SGC0946-treated groups. The data are presented as the mean ± SD of biological triplicates. Significance was determined by unpaired two-tailed Student's *t*-test. $^{****}P < 0.0001$.

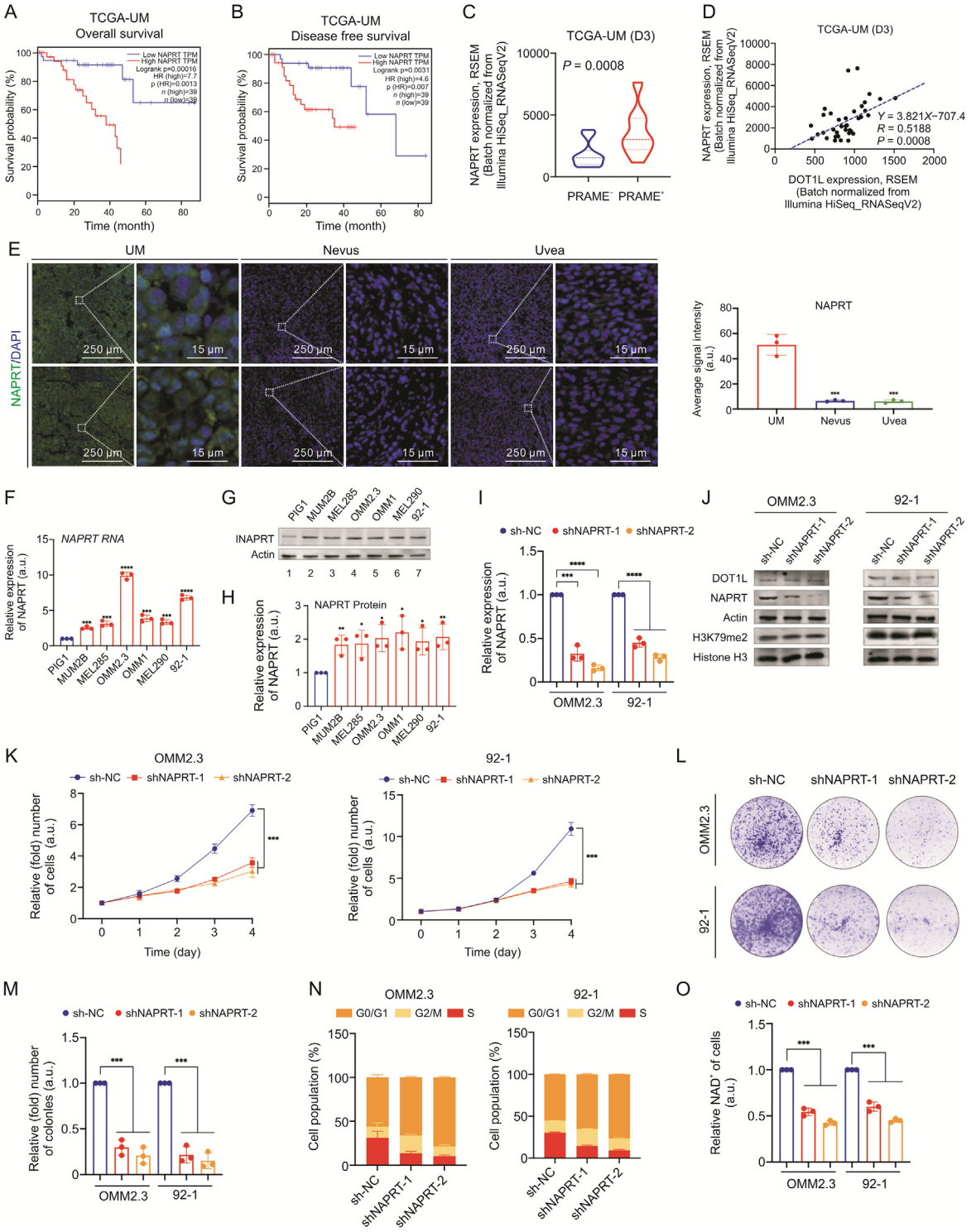

Fig. 6. Nicotinate phosphoribosyltransferase (NAPRT) functioned as an oncogene in uveal melanoma (UM). (A, B) Kaplan-Meier analysis of the correlations between NAPRT expression and overall survival (A) and disease-free survival (B) in the Cancer Genome Atlas (TCGA)-UM patients stratified by the NAPRT expression level: high (top 50th percentile, $n = 39$) and low (bottom 50th percentile, $n = 39$). Significance was determined by a two-sided log-rank test. (C) Comparison of NAPRT expression between the groups with high preferentially expressed antigen in melanoma (PRAME) expression ($n = 19$) and with low PRAME expression ($n = 19$) in TCGA-UM cohort of disomy 3 (D3) ($n = 38$). The violin plot shows the interquartile ranges (lines) and the observed number (width). Significance was determined by unpaired two-tailed Student's *t*-test. (D) Correlation analysis of RNA expression between NAPRT and disruptor of telomeric silencing 1-like (DOT1L) in TCGA-UM cohort of disomy 3 ($n = 38$). Significance was determined by *Pearson* correlation analysis ($R = 0.5188$, $P = 0.0008$). (E) Immunofluorescence of NAPRT (green) and 4',6-diamidino-2-phenylindole (DAPI) (blue) in UM samples and normal samples (nevus and uvea tissues). Representative images from three biological specimens are shown. Statistical histogram of the NAPRT immunofluorescence staining data in UM samples and normal samples (nevus and uvea tissues). The data are presented as the mean ± standard deviation (SD) of biological triplicates. Significance was determined by unpaired two-tailed Student's *t*-test. $^{***}P < 0.001$. (F) Real-time polymerase chain reaction (PCR) data showing the NAPRT expression in UM cells relative to that in PIG1 cells. The data are presented as the means ± SD of experimental triplicates. Significance was determined by unpaired two-tailed Student's *t*-test. $^{***}P < 0.001$, $^{****}P < 0.0001$. (G) Western blotting of NAPRT relative to β-actin (ACTB) in UM cells and normal melanocytes. The data are representative of experimental triplicates. (H) Densitometric analysis showing the protein expression level of NAPRT relative to that of ACTB in UM cells and normal melanocytes. The data are presented as the mean ± SD of experimental triplicates. Significance was

deficient cells. The intracellular NAD^+ level was significantly decreased in NAPRT knockdown cells (Fig. 6O). Consistently, the NAD^+ level was reduced in SGC0946-treated cells and DOT1L-deficient cells (Figs. S10A and B), indicating that NAPRT served as an oncogenic driver by modulating intercellular NAD^+ levels.

3.6. H3K79me2 promoted UM through NAPRT

To determine the function of NAPRT in DOT1L-mediated oncogenesis, we have re-introduced NAPRT after inhibiting DOT1L in UM cells (Fig. S11). As a result, NAPRT overexpression partially rescued the anticancer effects of SGC0946 treatment or DOT1L knockdown, including cell growth (Figs. 7A and B) and colony formation (Figs. 7C and D) capacities. Interestingly, the NAPRT overexpressed cells were more resistant to DOT1L inhibition (Figs. 7A–D), indicating that NAPRT served as an important downstream regulator of DOT1L-guided oncogenic events. Consistently, the NAD^+ level was restored after reintroducing NAPRT in DOT1L inhibited UM cells (Figs. 7E and F). Collectively, we unveiled a novel oncogenic DOT1L/NAPRT signaling axis that bridged metabolic reprogramming and transcriptional addiction in UM.

4. Discussion

Loss of histone methylation homeostasis is a crucial feature of cancer because it disrupts the normal landscape of gene expression, including the activation of oncogenes and the inactivation of tumor suppressors [24]. Herein, our results revealed a global histone methylation pattern in UM, identified novel DOT1L-guided transcriptional dysregulation in UM, and underscored the effect of this dysregulation on *NAPRT* expression and NAD^+ synthesis. Targeted correction of abnormal DOT1L expression through DOT1L silencing or treatment with molecular drugs considerably inhibited tumorigenesis, therefore leading to the identification of a novel strategy for targeting histone methylation in tumor progression.

DOT1L is the only recognized histone methyltransferase and catalyzes all the mono-, di-, and tri-methylation of H3K79 [25,26]. DOT1L participates in the tumorigenesis of multiple solid and hematologic malignancies [27–30]. For example, DOT1L fuses with mixed lineage leukemia (MLL) and regulates H3K79 methylation to maintain leukemic gene expression by suppressing sirtuin 1-regulated epigenetic silencing in MLL-rearranged leukemia [31]. Through interaction with the c-Myc-p300 complex, DOT1L accelerates H3K79 methylation and epigenetically activates epithelial-mesenchymal transition (EMT) mediators in breast cancer [32]. The DOT1L inhibitors EPZ004777, EPZ5676, and SGC0946 exert selective anti-tumor effects against MLL-rearranged leukemia [33–35] and suppress tumorigenesis in multiple cancers including multiple myeloma, lung cancer, colorectal cancer, and neuroblastoma [36–39]. EPZ004777, the first identified inhibitor, acts by competing with the cofactor SAM, which is indispensable for DOT1L methyltransferase activity, but it exhibits poor pharmacological properties [34]. A second-generation drug, EPZ5676, presents good toleration in a phase I study, inducing two patients' complete remission of 51 MLL-rearranged leukemia patients; however, its low bioavailability may contribute to its low response rates [40]. Subsequently, modifications to EPZ00477 resulted in the synthesis of SGC0946, although the effect of SGC0946 compared with EPZ00477 and EPZ5676 is currently unclear. Here, for the first time, we found selective anti-tumor efficacy of DOT1L inhibitors and revealed that SGC0946 served as the safest and most efficient DOT1L inhibitor for UM treatment.

The emerging concept of transcriptional addiction refers to the dysregulation of transcriptional programs in cancer that leads to the dependence of cancer cells on certain gene expression regulators [41]. These dependencies can endow cancer cells with increased sensitivity to inhibitors of certain regulators compared with normal cells, highlighting a novel therapeutic strategy in cancer. DOT1L was demonstrated to be a trigger of transcriptional addiction in leukemia. Specifically, MLL-AF fusion proteins in MLL recruit the histone methyltransferase DOT1L to the transcription factors (TF) homeobox A9 and Meis homeobox 1; thus, histone hypermethylation drives aberrant transcription of TF genes and leukemogenesis [42]. Our results indicated a novel mechanism of DOT1L-guided transcriptional addiction in UM.

We combined CUT&Tag data and RNA-seq data and found that only 13 genes with H3K79me2 were enriched at the promoter and downregulated after SGC0946 treatment, which might contribute to the following reasons. First, the function of DOT1L is not limited to H3K79 methylation. For example, DOT1L-governed transcription elongation and cell fate determination are reported to be independent of H3K79 methylation [43]. Second, in addition to transcriptional regulation, H3K79 methylation plays a crucial role in telomeric silencing, DNA damage response and cell cycle regulation [44–46]. Moreover, SGC0946 cannot completely inhibit the activity of DOT1L. Taken together, these factors might explain why only 13 genes were captured following the CUT&Tag and RNA-seq assays.

NAPRT, an intracellular enzyme, catalyzes the first step of NAD^+ biosynthesis from nicotinic acid [47]. NAPRT exhibits a striking rate of amplification in multiple cancers; specifically, NAPRT amplification was present in over 15% of the patients in TCGA-UM cohort [48]. NAD^+, a fundamental signaling cofactor, mediates cancer metabolism via multiple processes, including cell differentiation, oxidative stress, cell proliferation, DNA repair, and redox regulation [49]. For example, NAD^+ acts as a coenzyme in glycolysis, oxidative phosphorylation, fatty acid metabolism and tricarboxylic acid cycle [50]. NAD^+ also participates in various signaling pathways, such as sirtuin-mediated deacetylation and poly (ADP-ribose) polymerase-mediated ADP-ribosylation, which are tightly connected with cell cycle progression, DNA damage repair, and EMT [51,52]. Herein, our study first identified NAPRT as a novel oncogene in UM, which delineates a novel oncogenic mechanism that bridges epigenetic regulation and metabolic reprogramming [53,54].

determined by unpaired two-tailed Student's *t*-test. $^*P < 0.05$, $^{**}P < 0.01$. (I) Real-time PCR data showing NAPRT expression in UM cells (OMM2.3 and 92-1) upon NAPRT knockdown. The data are presented as the mean ± SD of experimental triplicates. Significance was determined by unpaired two-tailed Student's *t*-test. $^{***}P < 0.001$. (J) Western blotting of NAPRT and DOT1L relative to ACTB and of dimethylation of histone H3 lysine 79 relative to histone H3 in UM cells (OMM2.3 and 92-1) upon NAPRT knockdown. (K) A cell counting kit-8 assay was performed to assess the proliferation of UM cells (OMM2.3 and 92-1) upon NAPRT knockdown. The data are presented as the mean ± SD of experimental triplicates. Significance was determined by unpaired two-tailed Student's *t*-test. $^{***}P < 0.001$. (L) A colony formation assay was performed to assess the growth of UM cells (OMM2.3 and 92-1) upon NAPRT knockdown. Representative images from three experimental replicates are shown. (M) Statistical analysis of the colony formation assay data in UM cells (OMM2.3 and 92-1) upon NAPRT knockdown. The data are presented as the mean ± SD of experimental triplicates. Significance was determined by unpaired two-tailed Student's *t*-test. $^{***}P < 0.001$. (N) Cell cycle phase distribution in UM cells (OMM2.3 and 92-1) upon NAPRT knockdown. The data are presented as the mean ± SD of experimental triplicates. Significance was determined by unpaired two-tailed Student's *t*-test. Specific data from the cell cycle analysis are provided in Fig. S9. (O) Measurement of the intracellular nicotinamide adenine dinucleotide (NAD^+) levels in UM cells (OMM2.3 and 92-1) upon NAPRT knockdown. The data are presented as the means ± SD of experimental triplicates. Significance was determined by unpaired two-tailed Student's *t*-test. $^{***}P < 0.001$.

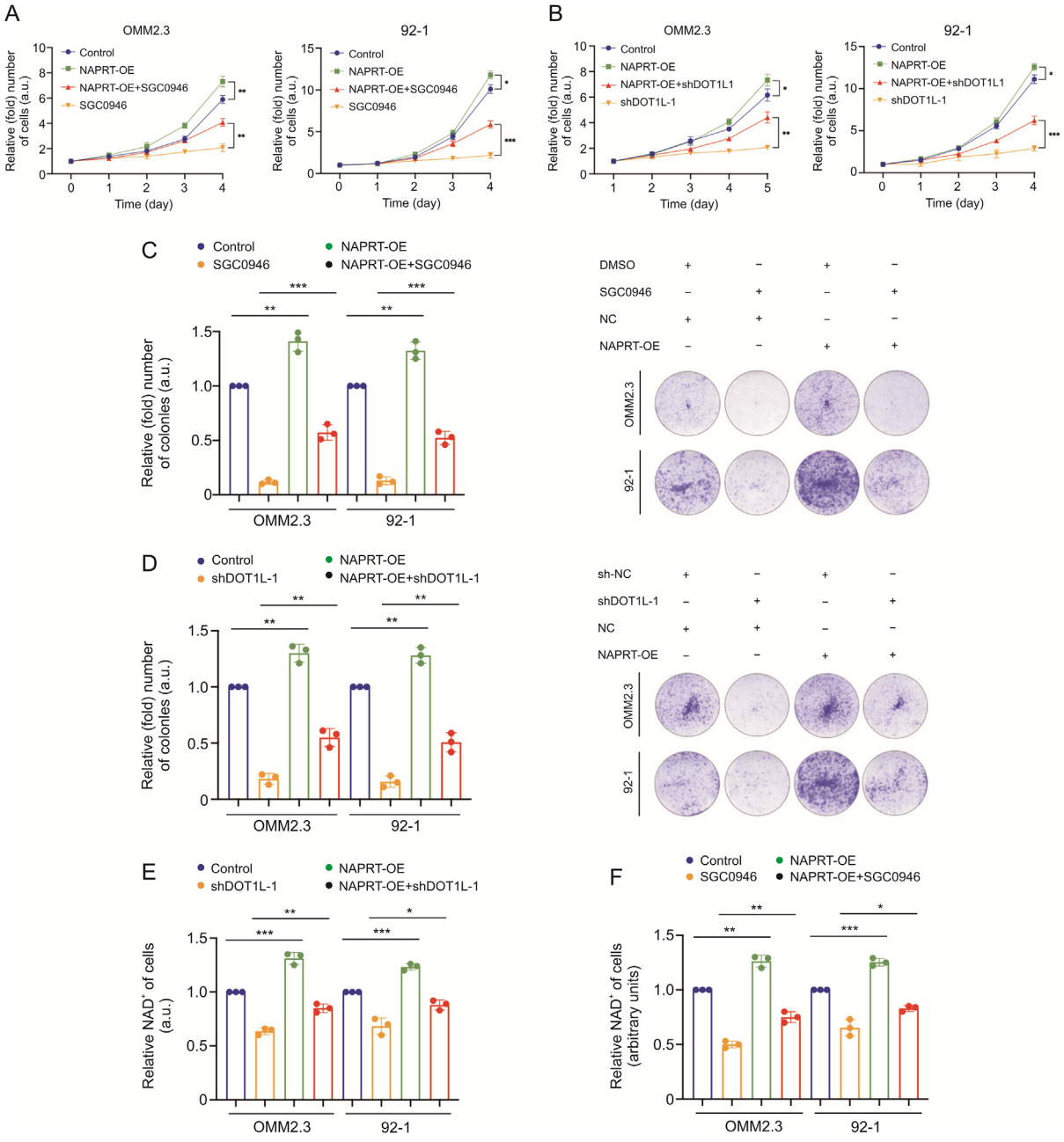

Fig. 7. The anticancer effects of disruptor of telomeric silencing 1-like (DOT1L) inhibitors or DOT1L knockdown were partially blocked by nicotinate phosphoribosyltransferase (NAPRT). (A) A cell counting kit-8 (CCK8) assay was performed to assess the proliferation of SGC0946-treated uveal melanoma (UM) cells (OMM2.3 and 92-1) upon reintroduction of NAPRT. The data are presented as the mean ± standard deviation (SD) of experimental triplicates. Significance was determined by unpaired two-tailed Student's *t*-test. $^{*}P < 0.05$, $^{**}P < 0.01$. (B) A CCK8 assay was performed to assess the proliferation of DOT1L-silenced UM cells (OMM2.3 and 92-1) upon reintroduction of NAPRT. The data are presented as the mean ± SD of experimental triplicates. Significance was determined by unpaired two-tailed Student's *t*-test. $^{*}P < 0.05$, $^{**}P < 0.01$, $^{***}P < 0.001$. (C) A colony formation assay was performed to assess the growth of SGC0946-treated UM cells (OMM2.3 and 92-1) upon reintroduction of NAPRT. Representative images from three experimental replicates are shown. The data are presented as the mean ± SD values. Significance was determined by unpaired two-tailed Student's *t*-test. $^{**}P < 0.01$, $^{***}P < 0.001$. (D) A colony formation assay was performed to assess the growth of DOT1L-silenced UM cells (OMM2.3 and 92-1) upon reintroduction of NAPRT. Representative images from three experimental replicates are shown. The data are presented as the mean ± SD values. Significance was determined by unpaired two-tailed Student's *t*-test. $^{**}P < 0.01$. (E) Measurement of the intracellular nicotinamide adenine dinucleotide (NAD^+) levels in DOT1L-silenced UM cells (OMM2.3 and 92-1) upon reintroduction of NAPRT. The data are presented as the means ± SD of experimental triplicates. Significance was determined by unpaired two-tailed Student's *t*-test. $^{*}P < 0.05$, $^{**}P < 0.01$, $^{***}P < 0.001$. (F) Measurement of the intracellular NAD^+ levels in SGC0946-treated UM cells (OMM2.3 and 92-1) upon reintroduction of NAPRT. The data are presented as the mean ± SD of experimental triplicates. OE: overexpression; NC: normal control. Significance was determined by unpaired two-tailed Student's *t*-test. $^{*}P < 0.05$, $^{**}P < 0.01$, $^{***}P < 0.001$.

5. Conclusions

In summary, by combining epi-drug screening and transcriptome analysis, our findings delineated an integrated picture of the histone methylation landscape in UM. First, we found that H3K79 methyltransferase was specifically upregulated. Moreover, UMs were much more sensitive to DOT1L inhibitors. Mechanistically, DOT1L facilitated H3K79me2 in the *NAPRT* promoter,

enhanced its expression, and induced an elevated NAD^+ synthesis in UM. Conclusively, our study unveiled a novel DOT1L/NAPRT oncogenic mechanism that bridges transcriptional addiction and metabolic reprogramming.

CRediT author statement

Xiang Gu: Methodology, Validation, Data curation, Investigation, Visualization, Writing - Original draft preparation; **Yu Hua**: Validation; **Jie Yu**: Methodology; **Ludi Yang**: Visualization; **Shengfang Ge**: Supervision, Project administration; **Renbing Jia**: Supervision, Funding acquisition; **Peiwei Chai**: Conceptualization, Visualization, Writing - Reviewing and Editing; **Ai Zhuang**: Data curation, Investigation, Writing - Reviewing and Editing; **Xianqun Fan**: Resources, Project administration, Supervision, Funding acquisition.

Declaration of competing interest

The authors declare that there are no conflicts of interest.

Acknowledgments

This work was supported by grants from Shanghai Key Clinical Specialty, Shanghai Eye Disease Research Center (Grant No.: 2022ZZ01003 to Xianqun Fan), the National Key Research and Development Plan (Grant No.: 2018YFC1106100 to Xianqun Fan), the National Natural Science Foundation of China (Grant Nos.: 12275178 to Shengfang Ge and 82103240 to Peiwei Chai), Innovative Research Team of High-level Local Universities in Shanghai (Grant Nos.: SHSMU- ZDCX20210902 to Renbing Jia and SHSMU-ZDCX20210900 to Xianqun Fan), the Science and Technology Commission of Shanghai (Grant No.: 19JC1410200 to Xianqun Fan), and Cross-disciplinary Research Fund of Shanghai Ninth People's Hospital, Shanghai Jiao Tong university School of Medicine (Grant No.: JYJC202210 to Ai Zhuang).

Appendix A. Supplementary data

Supplementary data to this article can be found online at https://doi.org/10.1016/j.jpha.2022.11.008.

References

[1] D. Hanahan, Hallmarks of cancer: New dimensions, Cancer Discov. 12 (2022) 31–46.
[2] J.C. Black, C. Van Rechem, J.R. Whetstine, Histone lysine methylation dynamics: Establishment, regulation, and biological impact, Mol. Cell. 48 (2012) 491–507.
[3] M. Esteller, Cancer epigenomics: DNA methylomes and histone-modification maps, Nat. Rev. Genet. 8 (2007) 286–298.
[4] G.G. Wang, L. Cai, M.P. Pasillas, et al., *NUP98-NSD1* links H3K36 methylation to Hox-A gene activation and leukaemogenesis, Nat. Cell Biol. 9 (2007) 804–812.
[5] E. Metzger, M. Wissmann, N. Yin, et al., LSD1 demethylates repressive histone marks to promote androgen-receptor-dependent transcription, Nature 437 (2005) 436–439.
[6] E. Kujala, T. Mäkitie, T. Kivelä, Very long-term prognosis of patients with malignant uveal melanoma, Invest. Ophthalmol. Vis. Sci. 44 (2003) 4651–4659.
[7] L. Khoja, E.G. Atenafu, S. Suciu, et al., Meta-analysis in metastatic uveal melanoma to determine progression free and overall survival benchmarks: An international rare cancers initiative (IRCI) ocular melanoma study, Ann. Oncol. 30 (2019) 1370–1380.
[8] A.G. Robertson, J. Shih, C. Yau, et al., Integrative analysis identifies four molecular and clinical subsets in uveal melanoma, Cancer Cell 32 (2017) 204–220.
[9] P. Chai, R. Jia, Y. Li, et al., Regulation of epigenetic homeostasis in uveal melanoma and retinoblastoma, Prog. Retin. Eye Res. (2021), 101030.
[10] T.M. Holling, M.W. Bergevoet, L. Wilson, et al., A role for EZH2 in silencing of IFN-gamma inducible MHC2TA transcription in uveal melanoma, J. Immunol. 179 (2007) 5317–5325.
[11] B. Jin, P. Zhang, H. Zou, et al., Verification of EZH2 as a druggable target in metastatic uveal melanoma, Mol. Cancer 19 (2020), 52.
[12] L.M. LaFave, W. Béguelin, R. Koche, et al., Loss of BAP1 function leads to EZH2-dependent transformation, Nat. Med. 21 (2015) 1344–1349.
[13] M. Schoumacher, S. Le Corre, A. Houy, et al., Uveal melanoma cells are resistant to EZH2 inhibition regardless of BAP1 status, Nat. Med. 22 (2016) 577–578.
[14] H.S. Kaya-Okur, S.J. Wu, C.A. Codomo, et al., CUT&Tag for efficient epigenomic profiling of small samples and single cells, Nat. Commun. 10 (2019), 1930.
[15] J.W. Harbour, M.D. Onken, E.D. Roberson, et al., Frequent mutation of BAP1 in metastasizing uveal melanomas, Science 330 (2010) 1410–1413.
[16] J.J. Bosch, J.A. Thompson, M.K. Srivastava, et al., MHC class II-transduced tumor cells originating in the immune-privileged eye prime and boost CD4(+) T lymphocytes that cross-react with primary and metastatic uveal melanoma cells, Cancer Res. 67 (2007) 4499–4506.
[17] P. Chai, J. Yu, R. Jia, et al., Generation of onco-enhancer enhances chromosomal remodeling and accelerates tumorigenesis, Nucleic Acids Res. 48 (2020) 12135–12150.
[18] R. Lin, S. Elf, C. Shan, et al., 6-Phosphogluconate dehydrogenase links oxidative PPP, lipogenesis and tumour growth by inhibiting LKB1-AMPK signalling, Nat. Cell Biol. 17 (2015) 1484–1496.
[19] M.G. Field, C.L. Decatur, S. Kurtenbach, et al., PRAME as an independent biomarker for metastasis in uveal melanoma, Clin. Cancer Res. 22 (2016) 1234–1242.
[20] G. Gezgin, S.J. Luk, J. Cao, et al., PRAME as a potential target for immunotherapy in metastatic uveal melanoma, JAMA Ophthalmol 135 (2017) 541–549.
[21] A. Barski, S. Cuddapah, K. Cui, et al., High-resolution profiling of histone methylations in the human genome, Cell 129 (2007) 823–837.
[22] S. Chowdhry, C. Zanca, U. Rajkumar, et al., NAD metabolic dependency in cancer is shaped by gene amplification and enhancer remodelling, Nature 569 (2019) 570–575.
[23] A. Basavapathruni, L. Jin, S.R. Daigle, et al., Conformational adaptation drives potent, selective and durable inhibition of the human protein methyltransferase DOT1L, Chem. Biol. Drug Des. 80 (2012) 971–980.
[24] E.M. Michalak, M.L. Burr, A.J. Bannister, et al., The roles of DNA, RNA and histone methylation in ageing and cancer, Nat. Rev. Mol. Cell Biol. 20 (2019) 573–589.
[25] Q. Feng, H. Wang, H.H. Ng, et al., Methylation of H3-lysine 79 is mediated by a new family of HMTases without a SET domain, Curr. Biol. 12 (2002) 1052–1058.
[26] D.J. Steger, M.I. Lefterova, L. Ying, et al., DOT1L/KMT4 recruitment and H3K79 methylation are ubiquitously coupled with gene transcription in mammalian cells, Mol. Cell Biol. 28 (2008) 2825–2839.
[27] M. Wong, P. Polly, T. Liu, The histone methyltransferase DOT1L: Regulatory functions and a cancer therapy target, Am. J. Cancer Res. 5 (2015) 2823–2837.
[28] Z. Zhou, H. Chen, R. Xie, et al., Epigenetically modulated FOXM1 suppresses dendritic cell maturation in pancreatic cancer and colon cancer, Mol. Oncol. 13 (2019) 873–893.
[29] L.Y. Bourguignon, G. Wong, M. Shiina, Up-regulation of histone methyltransferase, DOT1L, by matrix hyaluronan promotes MicroRNA-10 expression leading to tumor cell invasion and chemoresistance in cancer stem cells from head and neck squamous cell carcinoma, J. Biol. Chem. 291 (2016) 10571–10585.
[30] X. Wang, H. Wang, B. Xu, et al., Depletion of H3K79 methyltransferase Dot1L promotes cell invasion and cancer stem-like cell property in ovarian cancer, Am. J. Transl. Res. 11 (2019) 1145–1153.
[31] C.W. Chen, R.P. Koche, A.U. Sinha, et al., DOT1L inhibits SIRT1-mediated epigenetic silencing to maintain leukemic gene expression in MLL-rearranged leukemia, Nat. Med. 21 (2015) 335–343.
[32] M.H. Cho, J.H. Park, H.J. Choi, et al., DOT1L cooperates with the c-Myc-p300 complex to epigenetically derepress CDH1 transcription factors in breast cancer progression, Nat. Commun. 6 (2015), 7821.
[33] S.R. Daigle, E.J. Olhava, C.A. Therkelsen, et al., Potent inhibition of DOT1L as treatment of MLL-fusion leukemia, Blood 122 (2013) 1017–1025.
[34] W. Yu, E.J. Chory, A.K. Wernimont, et al., Catalytic site remodelling of the DOT1L methyltransferase by selective inhibitors, Nat. Commun. 3 (2012), 1288.
[35] S.R. Daigle, E.J. Olhava, C.A. Therkelsen, et al., Selective killing of mixed lineage leukemia cells by a potent small-molecule DOT1L inhibitor, Cancer Cell 20 (2011) 53–65.
[36] M. Wong, A.E.L. Tee, G. Milazzo, et al., The histone methyltransferase DOT1L promotes neuroblastoma by regulating gene transcription, Cancer Res. 77 (2017) 2522–2533.
[37] K. Ishiguro, H. Kitajima, T. Niinuma, et al., DOT1L inhibition blocks multiple myeloma cell proliferation by suppressing IRF4-MYC signaling, Haematologica 104 (2019) 155–165.
[38] L. Yang, Q. Lei, L. Li, et al., Silencing or inhibition of H3K79 methyltransferase DOT1L induces cell cycle arrest by epigenetically modulating c-Myc expression in colorectal cancer, Clin. Epigenet. 11 (2019), 199.
[39] W. Kim, R. Kim, G. Park, et al., Deficiency of H3K79 histone methyltransferase Dot1-like protein (DOT1L) inhibits cell proliferation, J. Biol. Chem. 287 (2012) 5588–5599.
[40] E.M. Stein, G. Garcia-Manero, D.A. Rizzieri, et al., The DOT1L inhibitor pinometostat reduces H3K79 methylation and has modest clinical activity in adult acute leukemia, Blood 131 (2018) 2661–2669.
[41] J.E. Bradner, D. Hnisz, R.A. Young, Transcriptional addiction in cancer, Cell 168 (2017) 629–643.

[42] C.W. Chen, S.A. Armstrong, Targeting DOT1L and HOX gene expression in MLL-rearranged leukemia and beyond, Exp. Hematol. 43 (2015) 673–684.
[43] K. Cao, M. Ugarenko, P.A. Ozark, et al., DOT1L-controlled cell-fate determination and transcription elongation are independent of H3K79 methylation, Proc. Natl. Acad. Sci. U. S. A 117 (2020) 27365–27373.
[44] Y. Huyen, O. Zgheib, R.A. Ditullio Jr., et al., Methylated lysine 79 of histone H3 targets 53BP1 to DNA double-strand breaks, Nature 432 (2004) 406–411.
[45] Y.H. Takahashi, J.M. Schulze, J. Jackson, et al., Dot1 and histone H3K79 methylation in natural telomeric and HM silencing, Mol. Cell. 42 (2011) 118–126.
[46] C.J. Janzen, S.B. Hake, J.E. Lowell, et al., Selective di- or trimethylation of histone H3 lysine 76 by two DOT1 homologs is important for cell cycle regulation in Trypanosoma brucei, Mol. Cell. 23 (2006) 497–507.
[47] V. Audrito, V.G. Messana, S. Deaglio, Nampt, Naprt, Two metabolic enzymes with key roles in inflammation, Front. Oncol. 10 (2020), 358.
[48] F. Piacente, I. Caffa, S. Ravera, et al., Nicotinic acid phosphoribosyltransferase regulates cancer cell metabolism, susceptibility to NAMPT inhibitors, and DNA repair, Cancer Res. 77 (2017) 3857–3869.
[49] Y. Zhu, J. Liu, J. Park, et al., Subcellular compartmentalization of NAD^+ and its role in cancer: A sereNADe of metabolic melodies, Pharmacol. Ther. 200 (2019) 27–41.
[50] A. Chiarugi, C. Dölle, R. Felici, et al., The NAD metabolome–a key determinant of cancer cell biology, Nat. Rev. Cancer 12 (2012) 741–752.
[51] J. Morales, L. Li, F.J. Fattah, et al., Review of poly (ADP-ribose) polymerase (PARP) mechanisms of action and rationale for targeting in cancer and other diseases, Crit. Rev. Eukaryot. Gene Expr. 24 (2014) 15–28.
[52] R.H. Houtkooper, E. Pirinen, J. Auwerx, Sirtuins as regulators of metabolism and healthspan, Nat. Rev. Mol. Cell Biol. 13 (2012) 225–238.
[53] N.N. Pavlova, J. Zhu, C.B. Thompson, The hallmarks of cancer metabolism: Still emerging, Cell Metabol. 34 (2022) 355–377.
[54] D. Hanahan, R.A. Weinberg, Hallmarks of cancer: The next generation, Cell 144 (2011) 646–674.